Journal of Fluids and Structures 18 (2003) 405–424

JOURNAL OF FLUIDS AND STRUCTURES

www.elsevier.nl/locate/jnlabr/yjfls

Numerical aspects of simulating the flow-induced oscillations of a rectangular bluff body

U. Bunge*, A. Gurr, F. Thiele

Department of Transport and Applied Mechanics, Technische Universität Berlin, Hermann-Föttinger-Institute of Fluid Mechanics, Sekr. HF1, Strasse des 17. Juni 135, D-10623 Berlin, Germany

Received 30 September 2002; accepted 21 July 2003

Abstract

The flow-induced oscillatory behavior of a rectangular body with a length-to-height ratio of $L/H = 2$ in incompressible, turbulent flow is numerically investigated at different Reynolds numbers based on the body length in a range between 2×10^4 and 12×10^4 at zero incidence. The body has one degree of freedom perpendicular to the mean-flow direction with a linear spring and linear damping. To compute the flow, a finite-volume based Navier–Stokes CFD-code is used, and a finite-difference-based algorithm is employed to solve the differential equation for the body vibration. The goals are the numerical simulation of an incident flow velocity at which resonance occurs, the exact determination of the physical mechanisms of the resonance, especially in the flowing medium, and a discussion of the numerical requirements to simulate the phenomenon. Key parameters of the overall model which exert influence on the quality of the simulation, e.g. turbulence modelling, time step and grid resolution, are examined. To achieve this aim, simulations with both steady and oscillating bodies are compared with experimental data and discrepancies are analyzed. Finally, an outlook on suggested future steps is given.

1. Introduction

The aim of the simulations is to determine the flow velocity at which a rectangular bluff body, Fig. 1, with a length-to-height ratio of $L/H = 2$ starts to oscillate at its natural frequency $f_0 = \sqrt{c/m}$ due to unsteady friction and pressure forces $F(t)$ acting on the body's surface. To compute the oscillatory motion $y(t)$ of the rectangular body, it is idealized as a point mass m on a bearing with linear damping d and stiffness c and one degree of freedom perpendicular to the mean-flow direction, as shown in Fig. 1, where U represents the mean flow velocity. The governing differential equation is given in Eq. (9).

The numerical results are compared to experimental results for Re-numbers $\mathrm{Re} = UL/v$ in a range between 2×10^4 and 12×10^4 (Ikenouchi et al., 1982), in which the natural frequency is $f_0 = 3.27$ Hz. The damping is very low with an attenuation factor or damping ratio of $D = d/(2mf_0) = 0.0032$. The Scruton number can be calculated with the given density ratio R_ρ to be $\mathrm{Sc} = 2Dm/(\rho H^2) = 4DR_\rho = 2.88$. For resonance to occur the excitation frequency must approach the natural frequency f_0, and the damping must be small, i.e. $D < 1/\sqrt{2}$. These parameters can be calculated based on an available analytical solution obtained for a harmonic excitation force given in Eq. (11).

This unsteady harmonic force results from a superimposed vortex street and vortex-edge interaction representing complex flow phenomena and cannot be computed analytically. Therefore, the flow must be computed numerically because it both influences and is influenced by the body's motion. A coupled solution becomes essential, especially when

*Corresponding author. Tel.: +49-30-314-22216; fax: +49-30-314-21101.
E-mail address: ulf.bunge@tu-berlin.de (U. Bunge).

0889-9746/$ - see front matter
doi:10.1016/j.jfluidstructs.2003.07.007

Nomenclature

ALE	arbitrary Lagrange–Euler
C_L	$= F/(\rho U^2 L)$, lift coefficient based on body length
C_D	drag coefficient based on body length
D	$= d/(2mf_0) = 0.0032$, attenuation factor
DES	detached eddy simulation
DFT	discrete Fourier transformation
DNS	direct numerical simulation
EARSM	explicit algebraic Reynolds stress model
EVM	eddy viscosity model
F	force acting on body due to pressure and friction
H	(= 0.13 m), height of body
L	(= 0.26 m), length of body measured in mean-flow direction
LLR	local linear realizable
LES	large eddy simulation
P	static pressure
P_k, P_ω	production terms in turbulence transport equations
(U)RANS(E)	(unsteady) Reynolds averaged Navier–Stokes (equation)
Re	$(= UL/\nu)$, Reynolds number based on body length
R_ρ	$m/(\rho HL) = 224.7$, density ratio (body/fluid)
S_{ij}	strain-rate tensor
SA	Spalart–Allmaras
SALSA	strain-adaptive linear Spalart–Allmaras
Sc	$(= 2Dm/(\rho H^2) = 4DR_\rho = 2.88)$, Scruton number
Sr	$(= f_{\mathrm{Sr}} H/U)$, Strouhal number
U	mean flow velocity
$U^{\partial V}$	velocity of volume boundary for moving grids
V	$(= U/f_0 H)$, normalized inflow or mean flow velocity, also volume in volume integrals
∂V	surface of volume for surface integral
Y^+	$\left(= l_n\sqrt{1/\nu \partial U_t/\partial Y_n}\right)$, normalized wall distance in boundary layer theory where t stands for tangential and n for normal to wall
c	linear stiffness of bearing
$c_{b1}, c_{b2}, c_{w1}, c_{w2}, c_{w3}, c_{v1}, \beta_\omega, \beta_k$	factors of turbulence models
d	linear damping of bearing
dA_i	component of face-normal vector for surface integration
f_0	$\left(= \sqrt{c/m} = 3.27\ \mathrm{Hz}\right)$, natural frequency of body oscillations
f_A	frequency of vortices impinging on trailing edge
f_D	$\left(= f_0\sqrt{1-D^2}\right)$, damped natural frequency
f_{Sr}	main frequency of lift-coefficient oscillations
f_m	maximum frequency resolved by chosen time step
f_t	modelled frequency
i	imaginary unit
$()_i$	vector component, $i = 1, 2, 3$ or x, y, z
k	turbulent kinetic energy
l	length scale in turbulent transport equations
l_n	wall-normal distance
m	(= 9.304 kg), mass of the body
$()_i'$	turbulent fluctuation of component
$\overline{u_i' u_j'}$	Reynolds stress tensor, averaged second moment of turbulent velocity fluctuations
t	time
$y(t)$	time-dependent excitation of body

Δt	time step
δ_{ij}	Kronecker Delta, unity tensor
κ	(= 0.41) von-Kármán constant
μ	fluid dynamic viscosity
ν	($= \mu/\rho$), fluid kinematic viscosity
ν_t	turbulent viscosity or eddy viscosity
$\tilde{\nu}$	turbulent viscosity in transport equations of one-equation models
ρ	density of fluid
ω	turbulent frequency

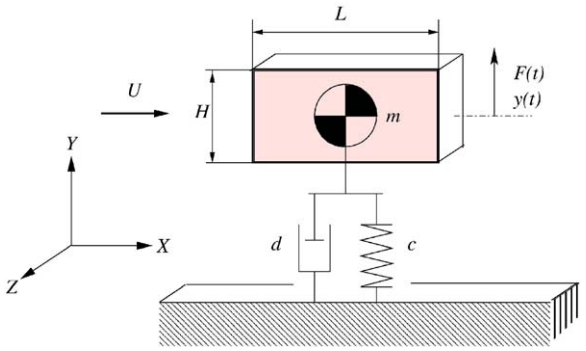

Fig. 1. Body and bearing, mechanical model.

excitation amplitudes are needed. Due to the fact that the body is not a streamlined shape and presents a blunt obstacle to the flow, unsteady vortices and complex three-dimensional flow structures emerging at the leading edge have to be represented by the numerical method. To obtain a quantitatively correct prediction in the frequency or time domain poses a significant challenge for any flow solver.

The shape of the body plays a predominant role in the resonance behavior because a simple Karman-vortex street with a pair of opposing eddies of equal size is not an adequate description of the flow phenomena (Sakamoto et al., 2000). Much longer bodies also cause eddies emerging at the leading edge, but they can impinge on the surface again downstream resulting in a reattachment of the flow followed by a subsequent separation at the trailing edge. In that case the frequency of the vortex shedding alone cannot serve to estimate the excitation frequency, as the impinging vortices add an extra force component acting at a different frequency than the wake vortex formation alone.

If the length-to-height ratio L/H slightly exceeds ≈ 2 (Deniz and Staubli, 1997), these eddies hit the trailing edge with a higher frequency than the vortex shedding. This can lead to earlier resonance, as shown in Fig. 2. For short bodies with $L/H < 2$, the leading edge vortices remain uninfluenced by the body shape and they alone make up the vortex street with a dominant frequency equal to that at which the vortices are shed.

In the case examined in this study with $L/H = 2$, a recirculation zone develops at the beginning of a leading edge vortex formation. Advancing in time, this leads to strong streamline curvature together with a maximum in lift. The arising force draws the body in the direction of the recirculation zone due to the lower pressure acting on that surface. The flow then partially impinges on the trailing edge causing a force opposing the lift and smaller secondary eddies with a higher frequency emerge at the trailing edge separation. Thus, as seen in Fig. 11, these impinging vortices reduce the lift to a certain amount, and occur at a frequency higher than vortex shedding $f_A > f_{\mathrm{Sr}}$, albeit, with a smaller amplitude. The discrete Fourier transformation of the time dependent lift coefficient consequently shows these distinct frequencies, Fig. 12. Due to the linearity of the differential equation Eq. (9) for the oscillating body both frequencies alone, i.e. f_{Sr} for vortex shedding and f_A for vortex impingement, can cause resonance. This means that, when $f_A \approx f_0$, i.e. the leading edge vortices impinge on the trailing edge with a frequency f_A close to the natural frequency f_0 of the body and its bearing, resonance will occur.

Obviously, in this case it is not sufficient to estimate the frequency of wake vortex formation f_{Sr} alone, which is also represented in the work by (Deniz and Staubli, 1997), where they evaluate the Strouhal number versus the elongation

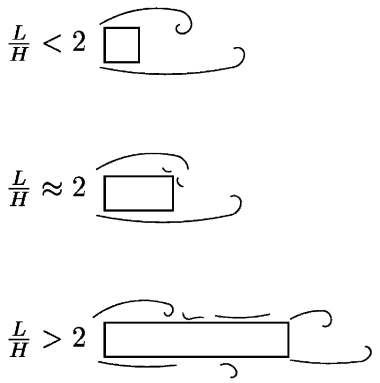

Fig. 2. Scheme of leading edge separation and vortices for different length-to-height ratios.

ratio L/H. In general it can be said that the highest frequency has to be used to compute the Strouhal number, if an estimation of the critical velocity is desired, and obviously, an estimation of the normalized resonance flow velocity with $V \approx 1/\mathrm{Sr}$ thus has to fail. It is also not possible to use galloping as an estimation as this phenomenon occurs even later at a higher mean flow velocity (Dowell, 1995).

Thus, the complex interaction between the flow and the body's (at first glance, simple) geometry cannot be easily estimated and poses a challenge for the flow mechanical solver, requiring an exact capturing of time and length scales over a wide range. There are at least two different frequencies with different amplitudes to resolve caused by emerging and impinging vortices at the leading and trailing edge. In order to capture this phenomenon it is essential to represent the length of the recirculation zone correctly, as this ensures the vortex impingement on the trailing edge.

For the lower frequencies of wake vortex formation f_{Sr} this is not as essential since interaction between the leading edge vortices and the trailing edge of the body does not influence this phenomenon. Therefore it is expected that the excitation at higher flow velocities, where the frequency f_A is already beyond the natural frequency f_0, can be computed correctly with less numerical effort.

2. Method

In this section, the numerical method is first briefly described followed by a detailed description of the code enhancements for computing the body's oscillations.

2.1. Fluid-mechanical solver

The flow is computed numerically using an in-house finite-volume-based code solving the unsteady and incompressible Reynolds-averaged Navier–Stokes (URANS) equations Eq. (1) in an implicit manner of first or, if desired, second-order accuracy in space and time. The momentum-conservation equation in an ALE formulation thus reads

$$\int_V \frac{\partial U_i}{\partial t}\,\mathrm{d}V + \oint_{\partial V} U_i(U_j - U_j^{\partial V})\,\mathrm{d}A_j = -\oint_{\partial V} \frac{P}{\rho}\,\mathrm{d}A_i + \oint_{\partial V} \nu\left(\frac{\partial U_i}{\partial x_j} + \frac{\partial U_j}{\partial x_i}\right) - \overline{u_i' u_j'}\,\mathrm{d}A_j, \tag{1}$$

where summation is implied over equal indices and all components are given in Cartesian coordinates. The Euler form ($U_j^{\partial V} = 0$, meaning that the surface of the control volume does not move) is used for the stationary body, whereas the grid is moved in a rigid-body-like manner according to the oscillations of the body, so that $U_j^{\partial V}$ directly corresponds to the velocity $\partial y/\partial t$ of the body as computed using Eq. (9). The fluid is treated as isothermal so that the viscosity can be kept constant and no transport equation for enthalpy or internal energy needs to be solved to compute the temperature. The Reynolds stresses $\overline{u_i' u_j'}$ arise in the averaging process and have to be modelled to avoid the solution of an additional six transport equations for the three-dimensional case.

All scalar quantities as well as the Cartesian components of tensorial quantities are stored in the cell centers of arbitrarily curvilinear, semi-structured grids that can capture complex geometries and allow local refinement. Moving and deforming grids are implemented by obeying the Space Conservation Law (Demirdžić and Perić, 1988; Bunge et al.,

2001). Diffusive terms are approximated with central schemes, whereas convective terms can be treated with central or upwind-biased limited schemes of higher order (Xue, 1998). The linearized equations are solved sequentially and the pressure is iterated to convergence using a pressure-correction scheme of the SIMPLE type that assures mass conservation because the pressure equation is derived from the continuity equation (Karki and Patankar, 1989).

A generalized Rhie and Chow interpolation is used to avoid an odd–even decoupling of pressure, velocity- and Reynolds-stress components (Obi et al., 1991). A variety of turbulence models featuring different degrees of complexity are implemented (algebraic, one- or two-equation models) to solve for the Reynolds stresses (Rung, 2000).

2.1.1. Turbulence models

The investigation is limited to two different one- and two different two-equation turbulence models. These are the Wilcox k–ω model (Wilcox, 1994), the SA-model (Spalart and Allmaras, 1992) and a modified version of each with variable coefficients, the LLR k–ω model (Rung and Thiele, 1996) and SALSA-model (Strain Adaptive, Linear SA model) (Rung et al., 2002). The modified versions are specifically tailored for non-equilibrium flows. These models have been used and validated in the context of fluid–structure interaction (Haase et al., 2002; Bunge et al., 2001); however, unsteady effects of higher frequency do not play such a dominant role in that cases.

EARSM have not yet been tested in this specific study, so that all models applied in this study rely on the isotropic or linear eddy-viscosity principle

$$\overline{u_i' u_j'} = \frac{2}{3} k \delta_{ij} - \nu_t \underbrace{\left[\left(\frac{\partial U_i}{\partial x_j} + \frac{\partial U_j}{\partial x_i} \right) - \frac{2}{3} \frac{\partial U_k}{\partial x_k} \delta_{ij} \right]}_{=2S_{ij}}. \tag{2}$$

An inherent error of Eq. (2) is the prediction of isotropic normal stresses $\overline{(u_1')^2} = \overline{(u_2')^2} = \overline{(u_3')^2}$ for plane, purely shear dominated flows where apart from, for example $\partial U_1/\partial x_2$ and $\partial U_2/\partial x_1$, all other components of the strain rate tensor vanish. In reality, these normal stresses differ by a factor in the range of 3–10 between the smallest and largest stress component in fully developed turbulent flows of that kind (Rung, 2000).

Another significant drawback of these kinds of models is the underlying assumption of a structural equilibrium for the Reynolds-stress tensor, which is a basic premise when trying to reduce the Reynolds-stress transport equations to an explicit expression connecting mean flow properties and turbulent fluctuations. Thus, streamline-curvature effects, if present, cannot be captured by these models as given (Moser and Moin, 1987). However, EVMs still play a predominant role and are very successful in CFD applications as long as these effects do not have a decisive influence. Moreover, their robustness, simple implementation and the relatively low computational cost preserves their popularity, whereas the use of more complex and computationally consumptive modelling techniques can only be justified by significant and foreseeable improvements.

One-equation models. The one-equation models used in this work are based on a transport equation straight for the turbulent viscosity ν_t. It reads in its non-conservative formulation for the SA model as

$$\frac{\partial \tilde{\nu}}{\partial t} + U_i \frac{\partial \tilde{\nu}}{\partial x_i} = c_{b1} \tilde{S} \tilde{\nu} + \frac{3}{2} \left[\frac{\partial}{\partial x_i} \left((\nu + \tilde{\nu}) \frac{\partial \tilde{\nu}}{\partial x_i} \right) + c_{b2} \left(\frac{\partial \tilde{\nu}}{\partial x_i} \right)^2 \right] - (c_{w1} f_w) \left(\frac{\tilde{\nu}}{l} \right)^2 \tag{3}$$

without the trip function included in the original version. A damping function is used to adjust ν_t in the near-wall region so that

$$\nu_t = \tilde{\nu} f_{v1}, \quad f_{v1} = \frac{X^3}{X^3 + c_{v1}^3}, \quad X = \frac{\tilde{\nu}}{\nu}, \quad c_{v1} = 7.1.$$

All other definitions and constants are given below for the modifications proposed previously by (Edwards and Chandra, 1996).

$$\tilde{S} = S \left(\frac{1}{X} + f_{v1} \right), \quad S = \sqrt{2 S_{ij} S_{ij}}, \quad f_w = g \left[\frac{1 + c_{w3}^6}{g^6 + c_{w3}^6} \right]^{1/6}, \quad g = r + c_{w2}(r^6 - r),$$

$$c_{b1} = 0.1355, \quad c_{b2} = 0.622, \quad c_{w1} = \frac{c_{b1}}{\kappa^2} + \frac{(1 + c_{b2})}{\sigma}, \quad \kappa = 0.41,$$

$$r = \tanh\left(\frac{\tilde{\nu}}{\kappa^2 l^2 \tilde{S}} \right) / \tanh(1), \quad c_{w2} = 0.3, \quad c_{w3} = 2, \quad \sigma = \tfrac{2}{3}.$$

The SALSA model is a modification by T. Rung (Rung et al., 2002) of the above that was inspired by (Menter, 1997). The main feature is a modified production term where the constant c_{b1} is enhanced by a function dependent on the

strain rate. Hence, the production term is sensitized to non-equilibrium effects because the modification primarily causes a reduction of production for excessive strain rates, and undesirable wall damping is suppressed.

Two-equation models. Both two-equation models are based on a transport equation for the turbulent kinetic energy k and a second equation for the turbulent frequency ω. The k-equation reads for both models

$$\frac{\partial k}{\partial t}+\frac{\partial U_i k}{\partial x_i}=P_k-\beta_k\omega k+\frac{\partial}{\partial x_i}\left(\left(\nu+\frac{\nu_t}{2}\right)\frac{\partial k}{\partial x_i}\right), \tag{4}$$

and the ω-equation is

$$\frac{\partial \omega}{\partial t}+\frac{\partial U_i \omega}{\partial x_i}=P_\omega-\beta_\omega\omega^2+\frac{\partial}{\partial x_i}\left(\left(\nu+\frac{\nu_t}{2}\right)\frac{\partial \omega}{\partial x_i}\right). \tag{5}$$

The models differ in the constants β and the representation of the production terms P_k and P_ω, i.e. in

$$P_k=c_\mu\frac{k}{\omega}S^2 \quad \text{and} \quad P_\omega=\alpha S^2 \tag{6}$$

the coefficients c_μ or α are determined in different ways, where the LLR k–ω version is a local linear two-parameter model derived from realizability and non-equilibrium turbulence constraints. The turbulent viscosity is determined for both models using

$$\nu_t=c_\mu\frac{k}{\omega}. \tag{7}$$

The coefficients of the stress-strain relation and the turbulence-transport equations are all functions of the non-dimensional invariants of the mean strain and vorticity rates. The approach tries to accomplish consistent stress-strain distributions not only in plane shear flow but also in more general flow situations.

2.1.2. DES approach

The three-dimensional computations were also performed using a non-zonal hybrid approach introduced as Detached Eddy Simulation (DES) in 1997 in order to combine the strengths of RANS and LES (Shur et al., 1999). It is implemented in the standard SA-model such that the length scale l in the eddy-viscosity transport equation is determined in the following way:

$$l=\text{MINIMUM}(l_n, C_{\text{DES}}\,\text{MAXIMUM}(\Delta_X,\Delta_Y,\Delta_Z)), \tag{8}$$

where Δ_J represents the local cell-width in the direction of the J-coordinate. The DES approach thus has a larger dissipation of eddy viscosity further away from the wall reducing the overestimated production since l is limited. This can be seen in the last term of Eq. (3), for example. Due to this additional dissipation, eddy viscosity is lowered, taking away some of the damping caused by turbulence or higher eddy viscosity.

In this case, no subgrid scale model is used and grid filtering is implied, requiring an unsteady, fully 3-D computation. The constant $C_{\text{DES}}=0.65$ is fixed in conjunction with centered differences (Spalart, 2001). It has to be mentioned that for the method to give good results, fine grids and small enough time steps are necessary, requiring experience and a thorough knowledge of the time and length scales involved in the specific case. In order to avoid the numerical dissipation of upwind-based schemes in the DES regions, a hybrid central/upwind approximation of the convective fluxes is used (Strelets, 2001).

An extension of the two-parameter modelling framework to DES is also possible and requires an alternative formulation of the dissipation in the k-equation. This is achieved by introducing a lengthscale proportional to the ratio $\sqrt{k}/\omega$. Then, the minimum of this length scale, the wall distance l_n, and the cell dimension are used to replace ω in the dissipation-term of the k-equation by a term proportional to the ratio of $\sqrt{k}$ and the appropriate length scale (Strelets, 2001). Thus, the turbulent frequencies used in the k-equation cannot become smaller than what can also be resolved by the grid. With this formulation the k dissipation is generally greater, leading to smaller turbulent viscosities to the same effect as previously mentioned for the one-equation models.

2.1.3. Computational grid

Several investigations in grid refinement and topology for the 2-D case showed that resolving the higher frequency of the leading-edge vortices impinging on the trailing edge requires a good grid resolution near the walls (see Fig. 3), whereas the lower frequency of the overall vortex shedding is best resolved by many points in the wake. In view of the high computation time for the unsteady calculations, a compromise between these two demands has to be found. Four different grids were initially created that consist of four blocks with orthogonal grid lines, as shown in Fig. 4. The boundary conditions applied are isothermal boundaries for all walls, inflow for blocks A, C and D, and convective

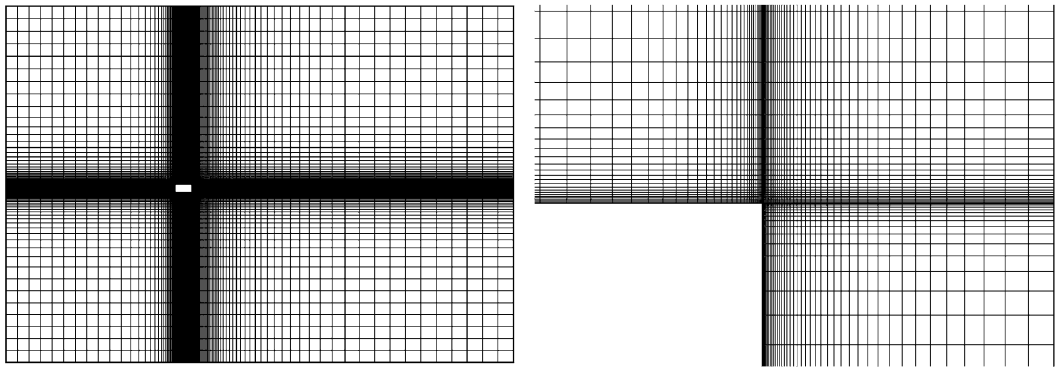

Fig. 3. Close up of computational grid (left) and detail of upper right trailing edge grid refinement in an area of $0.5H \times 0.37H$ (right).

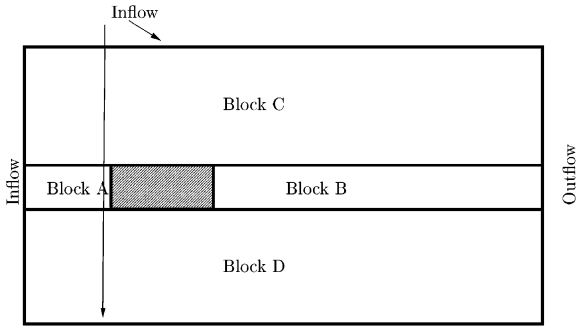

Fig. 4. Block structure, boundary conditions.

Table 1
Rough number of grid volumes and their partitioning

Grid volumes	Block A	Block B	Blocks C,D
15.000	30×27	80×27	150×40
24.000	30×27	120×27	190×50
36.000	50×47	100×47	235×60
46.000	60×37	190×37	300×60

outflow ensuring global mass conservation for blocks B, C and D. On the inflow boundaries a constant and homogeneous velocity is given. The grid is refined towards all walls so that $Y^+ \leqslant 1$ for the grid lines closest to the walls for any inflow velocity in order to fulfill the Low-Re constraints for the turbulence models.

Based on the assumption that the higher frequency of the force oscillation is dominated by the flow structure close to the body rather than by the vortex street, a dense grid around the body with a total of roughly 36 000 control volumes is chosen at the expense of the wake resolution, as shown in Table 1. Consequently, the back flow and impinging eddies on the trailing edge are well resolved whereas the flow structures in the wake can be only poorly resolved. The influence observed is that a higher resolution around the body, necessary to render f_A adequately, leads to a smaller frequency f_{Sr} of vortex shedding. It has to be mentioned that the treatment of convective terms is equally decisive and that central-difference schemes are to be preferred.

For the very few preliminary 3-D computations, two different grids are used. The 2-D grid is simply extended in the third dimension using 20 layers spanning $0.5L = H$. The first is an extension of the 36 000 control volume grid in the third dimension. The second, a finer grid with 25 layers consisting of 70 000 control volumes each, resulting in a total of roughly 1 800 000 volumes, is currently under examination. Periodic boundary condition is chosen in the third dimension to enable structures with a dimension of multiples of H to develop.

2.2. Structural-mechanical solver

The linear differential equation for the oscillation of the body,

$$m\frac{\partial^2 y}{\partial t^2} + d\frac{\partial y}{\partial t} + cy = F, \tag{9}$$

is discretized using third-order accurate finite differences for the derivatives with respect to time, $\partial^2 y/\partial t^2$ and $\partial y/\partial t$. The points used are y_{m+1} (forward time), y_m and k points y_{m-k} (backward time), and it is necessary to use $k = (1, 2, 3)$ to achieve third-order accuracy for $\partial^2 y/\partial t^2$. The procedure is simplified by the fact that the problem is solved using a constant time step Δt. Applying a Taylor-series expansion one gets

$$y_{m+1} = \frac{-1}{\left(\frac{11m}{12(\Delta t)^2} + \frac{d}{3\Delta t}\right)}\left[y_m\left(\frac{-5m}{3(\Delta t)^2} + \frac{d}{2\Delta t} + c\right) + y_{m-1}\left(\frac{m}{2(\Delta t)^2} - \frac{d}{\Delta t}\right) + y_{m-2}\left(\frac{m}{3(\Delta t)^2} + \frac{d}{6\Delta t}\right) - y_{m-3}\left(\frac{m}{12(\Delta t)^2}\right) - F_m\right], \tag{10}$$

and an explicit computation of the instantaneous amplitude at time step $m+1$ is possible with a given force F_m obtained from the pressure and friction on the body at time step m. This procedure is implemented in the fluid-mechanical solver described in the previous sections achieving loose coupling.

An analytical solution is available for a harmonic excitation given by $F = A\mathrm{e}^{\mathrm{i}\Omega t}$:

$$y(t) = Y[\mathrm{e}^{-f_0 D t}\cos(f_D t + \varphi)] + A\left[\frac{1}{c}\alpha(\Omega)\cos(\Omega t - \delta(\Omega))\right], \tag{11}$$

where φ denotes the phase shift that has to be computed from initial conditions together with the constant Y, and

$$\alpha(\Omega) = \frac{1}{\sqrt{(1-\eta^2)^2 + 4D^2\eta^2}},$$

$$\eta = \frac{\Omega}{f_0}, \quad \delta(\Omega) = \arctan\left(\frac{2D\eta}{1-\eta^2}\right). \tag{12}$$

Therefore, the numerical implementation can be successfully validated against analytical solutions and a variation of time steps gives an exact reduction of the deviation in comparison to the analytical solution according to the order of the scheme. In Fig. 5, the analytical results for a free and damped oscillation from an initial position not in equilibrium are depicted. The analytical and numerical solutions are almost congruent, because the time-step size was chosen to be small.

Some numerical damping can be observed, which has also been reported by others, e.g. (Semler et al., 1996) in application to nonlinear differential equations. As the same time step is chosen for the solution of both the fluid-mechanical and the structure-mechanical problem, and the flow solution requires a much higher temporal resolution, the time step is very small compared to the natural frequency of the structure. Therefore, this numerical damping is negligible. Moreover, the time-step size is small enough so that the given numerical order of accuracy is sufficient to resolve the oscillations.

2.3. Coupling procedure

The principle of the coupling procedure is shown in Fig. 6. By taking the sum over all normal and shear stresses acting on the body in the direction of the oscillatory degree of freedom, the excitation force is known at time t. This force is used (Step 1 in Fig. 6) to compute the amplitude for $t + \Delta t$ with Eq. (10) (Step 2). The whole computational grid is then moved according to the amplitude of motion, and the grid fluxes are computed (Step 3) so that the flow solution for $t + \Delta t$ can be computed (Step 4). Despite the higher orders of the structure and fluid mechanical solvers independently, this procedure is explicit in time and involves only a loose coupling of first order (Piperno et al., 1995). Nonetheless, due to the very fine time step necessary this accuracy is considered sufficient and discrepancies between experiments and results are shown to be influenced by other effects.

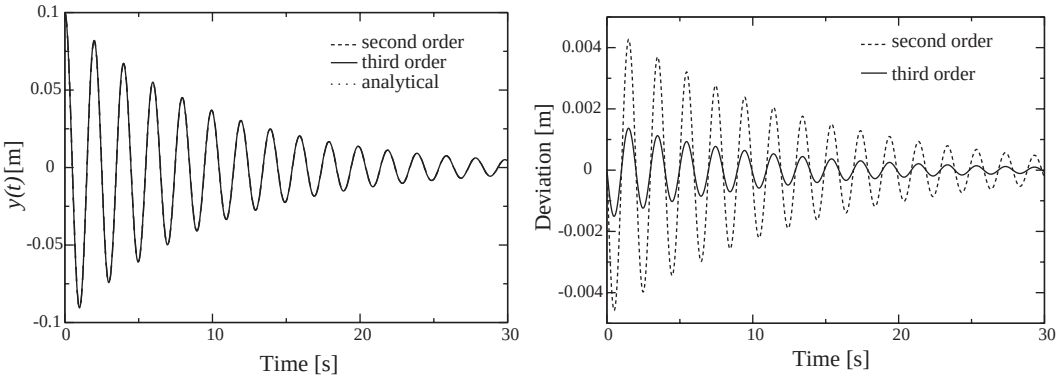

Fig. 5. Comparison of amplitudes of motion for different solutions of free oscillation.

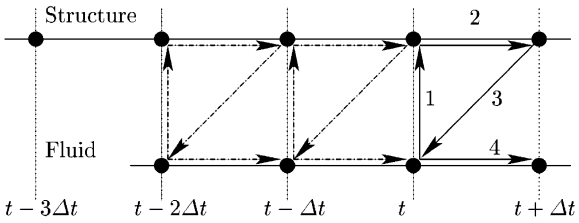

Fig. 6. Coupling procedure.

3. Results

Results are presented for two- and three-dimensional computations (2-D and 3-D, respectively); however, coupled solutions have thus far been obtained for the 2-D cases only. In the results that follow, the normalized inflow velocity V given as a parameter is proportional to the Reynolds number where $V = 3.0$ corresponds to $\mathrm{Re} = 2 \times 10^4$. The angle of attack is 0° and the length to height ratio is $L/H = 2$. The level of inflow turbulence intensity was kept below 1%.

3.1. 2-D computations, stationary body

A basic premise for good results from the coupled solutions is that the simulation of the flow has to be as accurate as possible in this case because the flow dominates the behavior of the coupled system. Therefore, to gain insight into the factors driving accurate flow modelling a study of influential parameters is completed for a stationary body with unsteady flow. The main goal is to define an adequate time step for the simulation that can capture the unsteady flow features causing the body to oscillate. Therefore, the Strouhal number computed with the time history of the lift coefficient is the best indicator for determining whether all the frequencies in the range of the natural frequency of the oscillation have been captured.

Fig. 7 shows a contour plot of an instantaneous velocity distribution revealing the strongly asymmetric and unsteady behavior of the flow that amounts to a vortex street with two dominating frequencies, i.e. two distinctive and opposing vortex pairs. The computation was done using the LLR k–ω turbulence model.

The lift and drag coefficients are shown in Fig. 8. The mean and time-dependent lift and drag coefficient C_L and C_D can be compared to experimental data, for example (Deniz and Staubli, 1997; Hémon and Santi, 2002). The mean lift coefficient is, of course, zero and the mean drag coefficient is computed to be 0.85 giving good agreement with experimental data. Moreover, the figure shows that the drag reaches its maximum together with the highest lift, whereas its minimum value corresponds to the dent in the lift curve. This corresponds to the vortex impinging the trailing edge, see Fig. 2, along with a parting of the vortex, such that part of the recirculating fluid on the surface of the body reduces the drag.

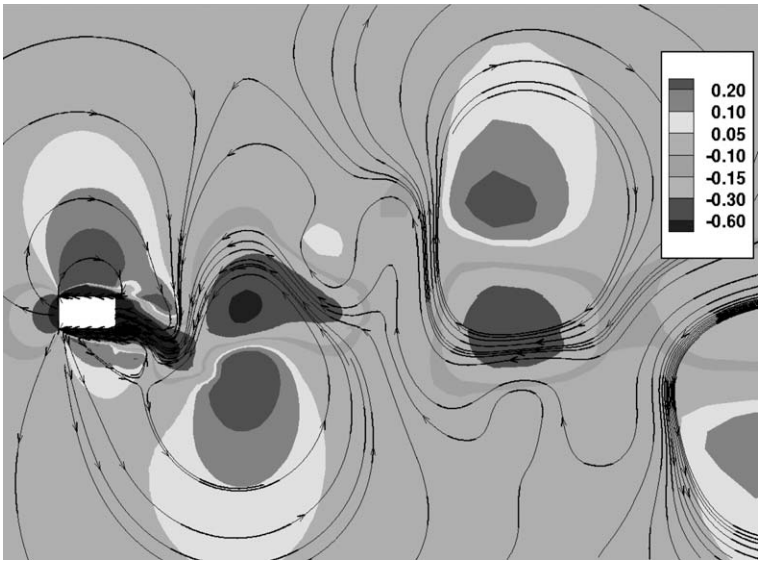

Fig. 7. Vortex street, relative velocity $(U_{\text{inflow}} - U(x,y))/U_{\text{inflow}}$ in mean flow direction and streamlines.

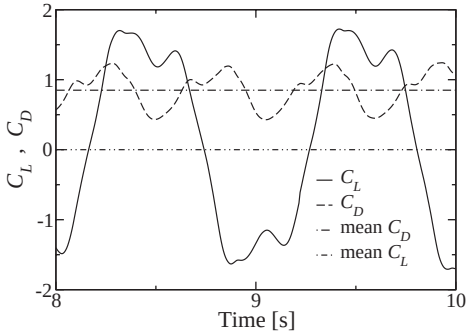

Fig. 8. Lift and Drag at $V = 5.5$, mean and time dependent values.

To illustrate the effect of vortex impingement, Fig. 9 shows the flowfield around the stationary body at different times. The corresponding lift coefficients are identified in Fig. 10, where (a) is not part of the detail as it is close to zero lift during lift increase. (b) marks the point with maximum lift where the flow is not influenced by the trailing edge, whereas for (c) and (d) the interference of the edge can be seen in the reduced flow velocity in the vicinity of the edge.

3.1.1. Variation of time step

The time step is varied four times for three different mean flow velocities V, and the LLR k–ω turbulence model is used. A significant difference in the lift-versus-time graph can be seen between the coarsest and finest time step, as shown in Fig. 11. The main detriment of a too coarse time step lies in the failed representation of the higher frequency that cannot be resolved by a coarser time step. This higher frequency corresponds to f_A and causes the dent in the peaks of the lift-versus-time curve, as shown in Fig. 10. Obviously, to capture this behavior it is essential to simulate the vortex impingement. Moreover, with a finer time step, the curve evolves more regularly, hinting at a better reproduction of the periodic nature of the phenomenon.

The computed Strouhal numbers, shown in Table 2, are too low compared to experimental data that usually give 0.08 (Deniz and Staubli, 1997) for a wide range of Reynolds numbers. Moreover, the Strouhal numbers differ depending on the time step. In this case, the experimentally determined Strouhal numbers (for vortex shedding only) are better captured using a coarser time step which is not adequate for computing f_A as already mentioned in context of the description of the numerical grids. The reason can be recognized in Fig. 11. If the time step is not sufficiently small to resolve f_A, the overall frequency f_{Sr} of vortex shedding that is used to compute the Strouhal number for Table 2, can

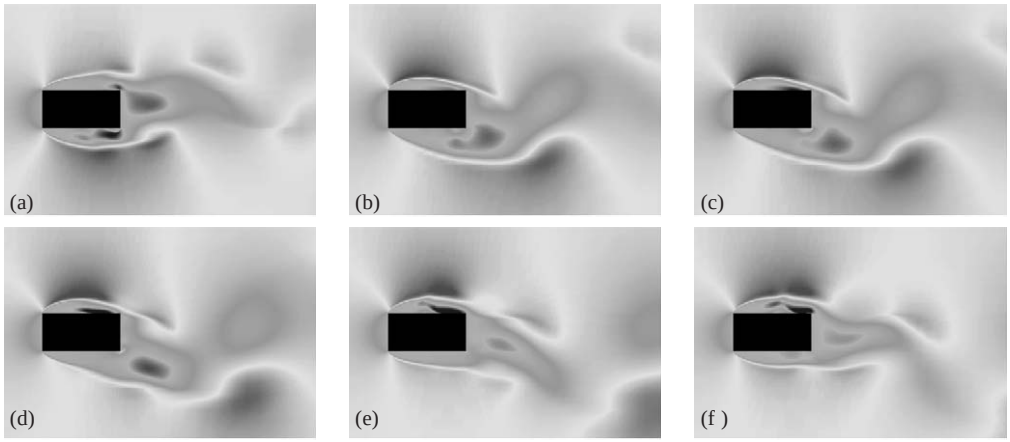

Fig. 9. Magnitude of flow velocity, influence of trailing edge on flow.

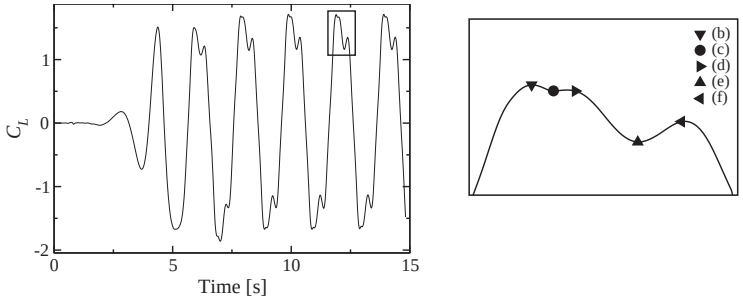

Fig. 10. Lift coefficient (left) and detail of dent in peak of Lift (right).

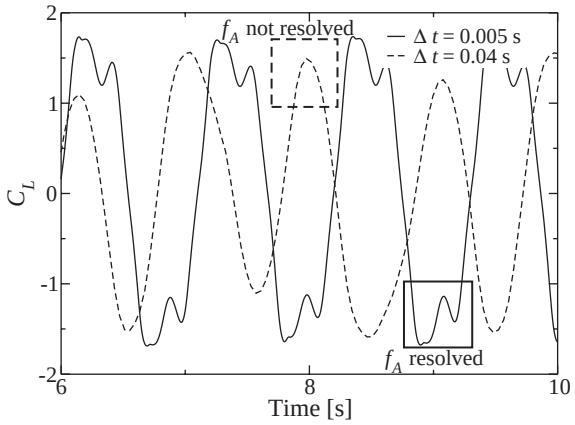

Fig. 11. Lift at $V = 5.5$, smallest and largest time step.

grow. Therefore, the convergence of the Strouhal number is not necessarily monotonic when the flow physics change due to the improved accuracy of the simulation.

Obviously, a constant time step is not applicable for all velocities. Rather, a constant normalized time step has to be chosen so that the physical time step is reduced with increasing flow velocity as f_{Sr} and f_A also increase. Choosing a constant normalized time step assures that a constant Strouhal number can be resolved equally with increasing Reynolds number in the given range.

Table 2
Variation of time step, resulting Strouhal numbers for different flow velocities

$\Delta t_{\mathrm{dim}}[s]$	$V = 3.0$ $\Delta t(U/H)$	Sr	$V = 5.5$ $\Delta t(U/H)$	Sr	$V = 15.0$ $\Delta t(U/H)$	Sr
0.005	0.05	0.055	0.092	0.053	0.25	0.057
0.01	0.1	0.055	0.183	0.050	0.5	0.055
0.02	0.2	0.057	0.366	0.061	1.0	0.054
0.04	0.4	0.062	0.732	0.067	2.0	0.033

The goal to render resonance for the coupled computations thus necessitates f_A to be resolved, which represents the impingement of leading edge vortices on the trailing edge. Resonance happens at a velocity $V < 1/\mathrm{Sr}$ and cannot be achieved by a too coarse time step. A normalized time step $\Delta t(U/H) = 0.1$ is found to be adequate for first-order time discretization of the flow computation with the code described previously to fulfill the aforementioned requirements.

An analysis of the frequencies exhibited by the lift coefficient time history is shown as a discrete Fourier transform (DFT) in Fig. 12, and three important points are identified: The constant natural frequency f_0 of the body and its bearing, the smaller frequency f_{Sr} of global vortex shedding and the higher superimposed frequency f_A that can obviously become critical for $6.0 < V < 9.0$. The critical velocity determined experimentally is roughly $V = 5.5$ (Ikenouchi, et al., 1982), and this result apparently cannot be captured by the 2-D simulation. However, the phenomenon can be simulated, but the frequency is too low because the predicted Strouhal numbers are already too small. Moreover, as shown in Fig. 22, for higher flow velocities, the galloping instability is very well reproduced, but at also a too small Strouhal number.

3.1.2. Variation of turbulence models

As shown in Fig. 13, the one-equation models are not capable of rendering the unsteadiness of the flow adequately, whereas the two-equation models exhibited sufficient unsteadiness, but differed in the frequency f_A. The LLR k–ω model exhibits the highest frequency and smoothest curve and is thus adopted for all of the remaining computations. The SA model does not exhibit any unsteady behavior in a reasonable time interval, whereas the SALSA model gives growing amplitudes. The results produced by the SA and SALSA models are not as periodic as desired and do not exhibit two distinct frequencies. This is a well-known weakness of the one-equation RANS modelling framework, restricting it to attached flows around streamlined bodies in aerodynamic applications, even though the one-equation models are successful and very efficient with respect to computing time and stability.

3.1.3. Frequency gap

A basic premise for applying the RANS equations to unsteady flows is a gap between resolved frequencies, such as f_A, and any modelled frequency, such as the turbulent frequency. This gap directly corresponds to the time period chosen for Reynolds averaging. The time step chosen for temporal discretization has to be sufficiently larger than the averaging period in order to ensure that a resolution of the modelled frequencies is avoided (Rung, 2000). This difference in the time scales can be expressed and validated in terms of a spectral or frequency gap between the maximum frequency f_m that can be resolved by the time step and the minimum frequency f_t modelled by the turbulence closure chosen.

To estimate a resolved frequency, one has to simply assume a number of time steps that are necessary for a given code of a certain order to map a complete period of an oscillatory curve, such as the sine curve. Based on the rough but conservative estimation that a period of $1/f_m$ can be represented by $n = 10$ points or time steps with $\Delta t(U/H) = 0.1$, this spectral gap can only be guaranteed very close to the wall where the turbulence models act almost as in steady state due to the very high turbulent frequencies compared to the mean flow unsteadiness, even if this mean flow unsteadiness is comparatively small like f_A in comparison to f_{Sr}.

This area is restricted to roughly 10 control volumes distance from the walls. Thus, an overlapping of turbulent and resolved frequencies occurs almost in the whole computational domain and not only in the wake. As an example to demonstrate the worst case, in Table 3, the smallest turbulent frequencies are given together with the distance from the rear wall in the wake where they occur. As a comparison, the maximum frequency presumedly resolved by $\Delta t(U/H) = 0.1$ at a given velocity is also stated. Consequently, a false reproduction of the energy spectra of turbulent and mean flow oscillations cannot be ruled out, but it is impossible to quantify the impact, all the more when the overall results remain correct (Lübcke et al., 2001).

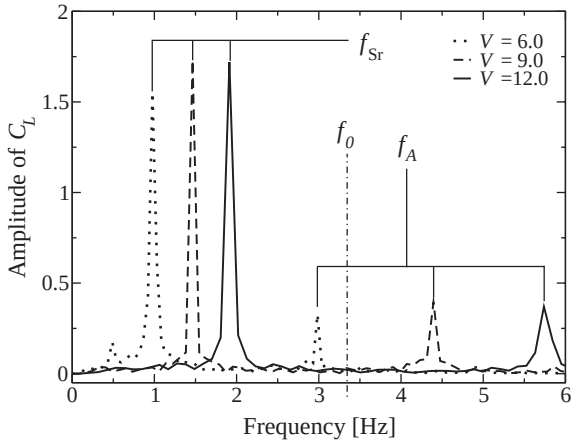

Fig. 12. DFT of lift for $\Delta t(U/H) = 0.1$, LLR k–ω, steady structure, observable frequencies.

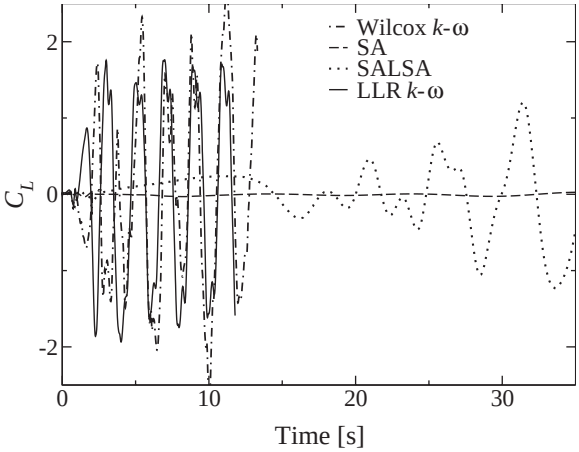

Fig. 13. Lift coefficient for different turbulence models.

Table 3
Spectral overlap using LLR k–ω turbulence model

V	f_m (Hz)	f_t (Hz)	l_n/H
3.0	9.8	0.045	16
5.5	18.0	0.165	15
6.0	19.6	0.186	16
9.0	29.4	0.374	11
12.0	39.2	0.671	7
15.0	49.0	0.853	8

Figs. 14 and 15 show instantaneous distributions of the ratio of turbulent to resolved frequencies f_t/f_m around the body for two different velocities with exemplary cuts to illustrate the data in Table 3. The figures depict the ratio on the cut versus normalized wall distance l_n/H.

In conclusion, conflicting purposes remain—resolving the oscillatory frequency f_A of the mean flow and not resolving any turbulent frequency f_t while maintaining a small time step to ensure the stability and accuracy of the solution method. Alternatively, the solution method for the flow could be changed completely to LES or DES at the expense of much higher computational costs.

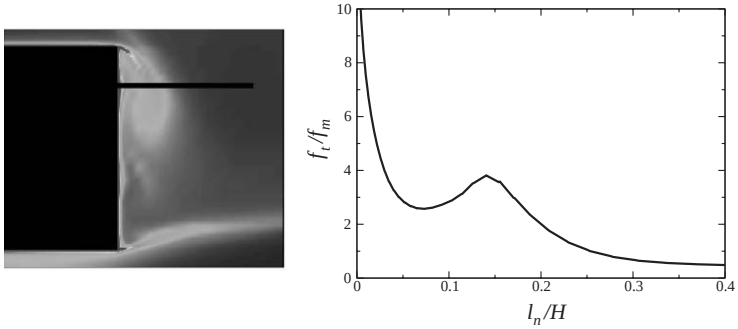

Fig. 14. Trailing edge, ratio of turbulent to resolved frequencies versus wall distance along cut.

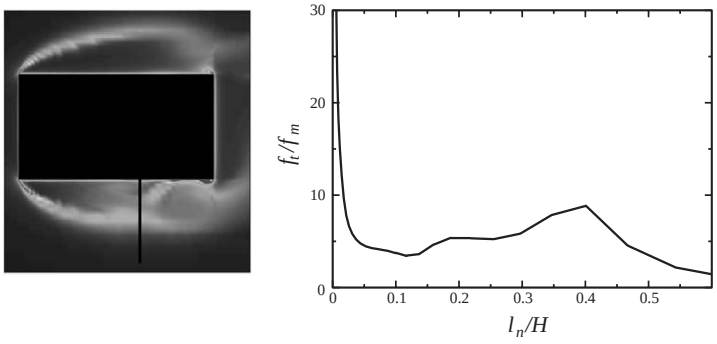

Fig. 15. Bottom edge, ratio of turbulent to resolved frequencies versus wall distance along cut.

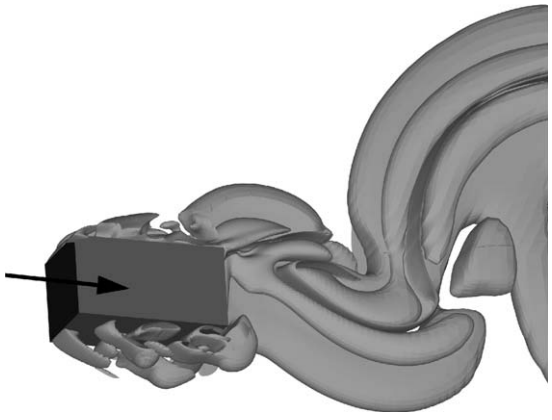

Fig. 16. Iso surfaces of instantaneous velocity in the third direction.

3.2. 3-D computations, stationary body

The 3-D DES did not yield the desired results with an improved representation of frequencies. However, 3-D effects are visible, as exemplified by Fig. 16. The iso surfaces of instantaneous velocity reveal non-tube-like structures in the upper wake region and close to the wall, indicating oscillations in the third direction. Though their wavelength is restricted due to the limited number of cells in that direction and the periodic boundary condition, the frequencies tend to become smaller using a 3-D instead of a 2-D simulation with the same turbulence model. Therefore, smaller time steps are essential. Although the primary frequency f_{Sr} becomes smaller and closer to the experimental results, the

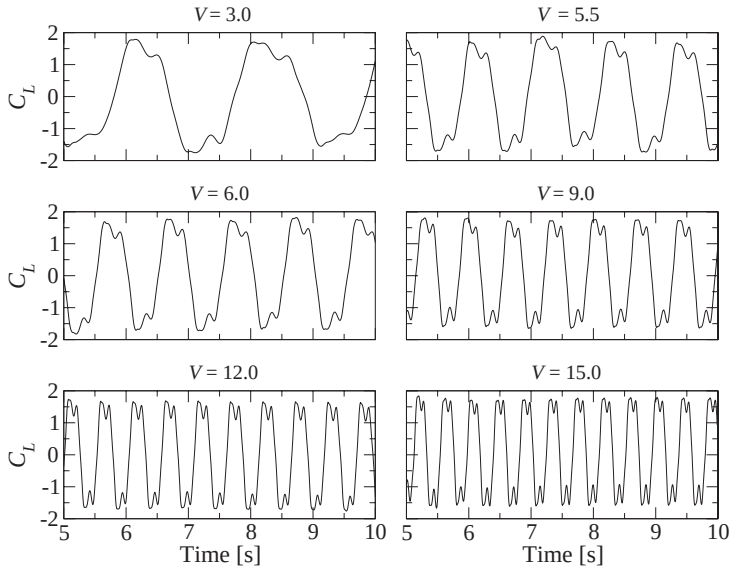

Fig. 17. Lift coefficient for oscillating body for different flow velocities.

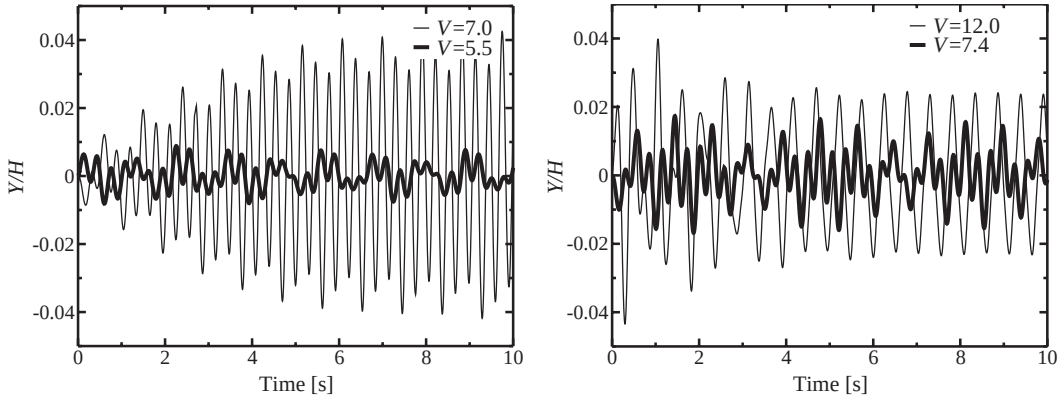

Fig. 18. Comparison of amplitudes of motion for different flow velocities.

oscillatory behavior does not show the regular and distinct separation of f_{Sr} and f_A as obtained with the 2-D computations.

It should be noted that the 3-D computations are very time consuming. With a cluster that consists of 22 Pentium II (400 MHz) PC's, one period of the *stationary* body took roughly 5 CPU-days during which the performance was approximately 70% for each processor. This high CPU load was achieved with a domain-decompositioned block-structured grid whose blocks could be made to be equal in size due to the simple geometry. In order to obtain reasonable results that can be time averaged or analyzed statistically or by Fourier analysis, computation times of up to several months are required *after* initial perturbations have subsided which itself can take a month. Long run times even on a faster PC cluster are required, and, therefore, parametric studies or more comprehensive investigations, e.g., in grid dependence, are still unfeasible for 3-D unsteady computations even if movement of the grid is not included.

3.3. 2-D computations, oscillating body

The computations described in this section are achieved using the LLR k–ω model in conjunction with a normalized time step of $\Delta t(U/H) = 0.1$ by restarting from an unsteady simulation of a stationary body with a regularly oscillating solution. This initial condition results in a rapid development of the coupled solution and allows one to determine whether a resonance is developing early during the solution computation. Comparing Fig. 17 with Fig. 11, it is clear

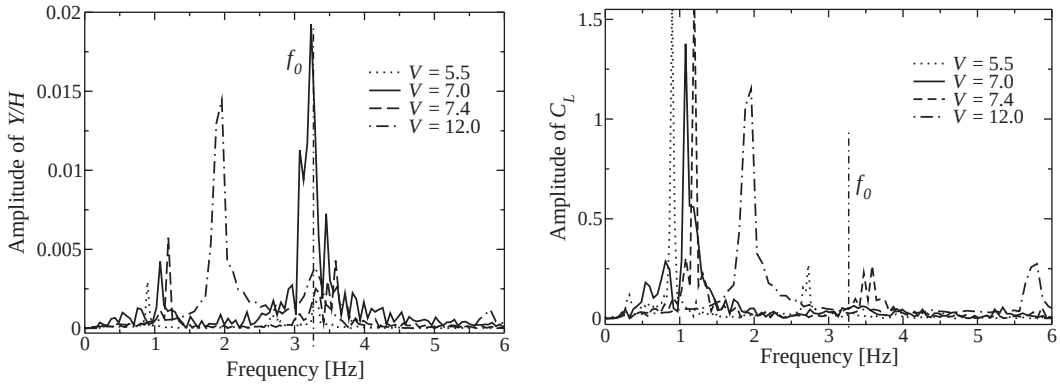

Fig. 19. Frequencies of motion (left) and lift coefficient (right) for different velocities.

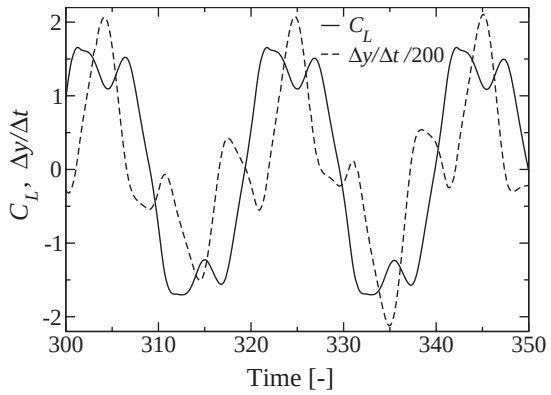

Fig. 20. Lift and temporal derivative of motion versus reduced time $t(U/H)$.

that the principal behavior of the flow does not significantly change compared to the stationary results. The lift curves remain uninfluenced, and the two dominant frequencies still occur. With higher flow velocity V, the frequencies grow, justifying the use of a normalized time step size as previously mentioned.

The range of mean flow velocities can be separated into two parts at a flow velocity slightly beyond the resonance velocity at $f_A = f_0$. The two experimentally found resonance velocities $V = 5.5$ and 12.0 can be assigned to each of these parts. In the first part the oscillations of the body are in phase with the lift force, whereas the oscillations are out of phase beyond the first resonance, as shown in Fig. 21. The numerical resonance velocity corresponding to the experimental $V = 5.5$ is slightly above $V = 7.0$, as revealed in the Fourier transforms in Fig. 19. Contrary to this discrepancy, the second resonance velocity is captured well, as shown in Fig. 22.

The evolution of amplitudes of motion for two flow velocities from these two parts are shown in Fig. 18 and the typical behavior of a body with a degree of freedom perpendicular to the flow with $L/H \approx 2$ is observable.

With increasing flow velocity, the displacement amplitude of the body increases first. After reaching resonance at $f_A = f_0$ ($7.0 < V_{\text{resonance}} < 7.4$) due to the impingement of leading edge vortices on the trailing edge, the amplitude decreases rapidly as the leading edge vortices do not hit the trailing edge for higher flow velocities. The excitation by the global vortex shedding due to leading edge separation ($V \approx 1/\text{Sr}$) slowly begins to prevail, resulting in the onset of galloping roughly at $V = 12.0$, Fig. 22.

In Fig. 19, it can be seen that the discrete Fourier transformed frequencies of the movement have a peak at f_0 for $V = 7.0$, which reveals that the body oscillates with f_0 due to $f_A \approx f_0$. Moreover, the peak in the amplitude of the lift is almost totally cancelled out at $V = 7.0$, which can also be seen in Fig. 21. This demonstrates that the body follows the vortices tending to avoid the impingement of these vortices on the trailing edge.

Although the vortex street forms the main unsteadiness in the mean flow with the highest amplitudes, these main oscillations of the lift at a frequency f_{Sr} have no influence up to that point and a little beyond until galloping starts. They

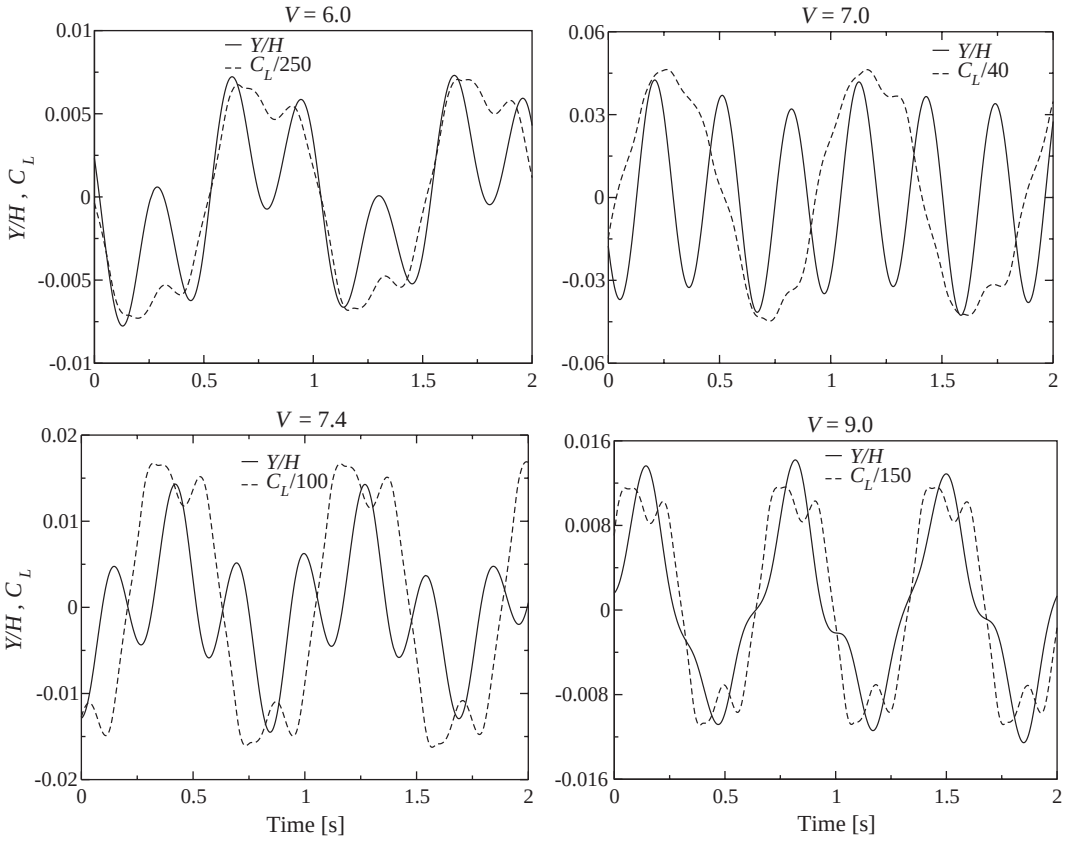

Fig. 21. Lift coefficient (scaled) and excitation versus time for different flow velocities.

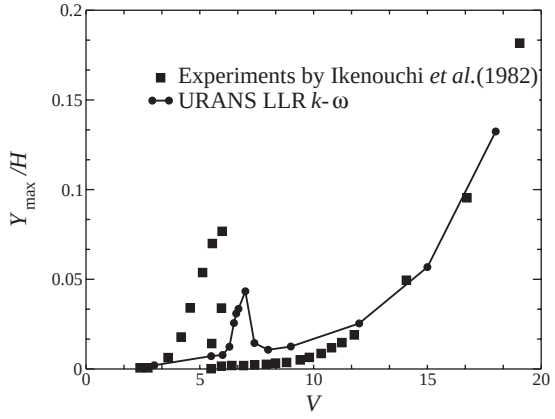

Fig. 22. Maximum amplitudes of motion versus flow velocity.

are, therefore, not responsible for this resonance. Increasing the velocity beyond $V = 7.4$ the natural frequency has been exceeded with $f_A > f_0$, and the amplitudes decrease, oscillating out of phase. This development is graphically demonstrated in Fig. 21. The largest amplitudes of motion occur for $V = 7.0$ and the lift curve is somewhat smoothed out by the movement of the body which oscillates almost regularly with f_A.

Fig. 19 depicts a high amplitude at $V = 12.0$ caused by f_{Sr} that increases with raising the flow velocity V. This galloping phenomenon can be estimated based on a galloping force model as presented in Hémon and Santi (2002). The

Scruton number can be calculated to be $Sc = 2Dm/(\rho H^2) = 4DR_\rho = 2.88$, and the time lag between the lift oscillations and first temporal derivative of the motion can be evaluated to be $\tau_r = \tau(U/H) = 3$, as shown in Fig. 20. The slope of the lift curve $\partial C_L/\partial\alpha$ dependent on the angle of attack is taken from (Deniz and Staubli, 1997). Then the following equation is evaluated:

$$\frac{V}{4\pi Sc} + \frac{2}{\partial C_L/\partial\alpha \cos(2\pi\tau_r/V)} = 0 \tag{13}$$

for V yielding $V = 12.0$. This result agrees well with the experimental and numerically found flow velocity. In evaluating Eq. (13), it is found that the parameter τ_r is the most influential. This means that it has to be computed very accurately because small deviations yield different results.

Comparing the amplitudes of motion to the experimental results, it is found that the maximum amplitude of oscillation computed numerically at $V = 7.0$ is roughly 4% of the body's height H whereas experiments or computations yield 8% at $V = 5.5$ (Ikenouchi et al., 1982; Anju et al., 1995) indicating that amplitudes and frequencies of the experiments for the first resonance are not captured quantitatively. Although the amplitudes might be increased by using another flow velocity $7.0 < V < 7.4$, the goal to reproduce the experimental resonance velocity is thus not yet achieved by the 2-D coupled computations. A comparison of experimental data and computations is presented in Fig. 22, where the experimental data show the same principal behavior dependent on the flow velocity. It can be seen that the agreement with experiments becomes better for higher velocities and becomes very good when galloping has begun.

4. Conclusions

The phenomenon of flow oscillations can be simulated with results that are qualitatively correct by the described procedure. The goal to reproduce the first experimental resonance velocity caused by vortex impingement on the trailing edge, however, is not yet achieved by the 2-D coupled computations and will not be achieved without changes in the modelling procedure for 2-D. To facilitate improvements in the modelling techniques, more experimental data predominantly in the time domain are needed to fully validate the procedure and to make more reliable comparisons.

Determining the reasons for the deviation from experiments can only be done in the scope of the varied parameters. Although all of the modelling parameters have not been investigated in this study, the most influential are clear: spatial and temporal discretization, numerical procedure, and physical models, especially for treating turbulence. However, to quantify the influences, a complete matrix of computations will ultimately be required. This extensive investigation is currently unfeasible in view of an average computation time of roughly 3.6 CPU minutes for one time step with 100 inner iterations on a Pentium III 600MHz for a 2-D testcase with 36.000 volumes (incompressible, two-equation turbulence model). As shown in this paper, the treatment of turbulence plays a dominant role and an enhanced predictive range including impinging or free shear flows and strong streamline curvature is a premise for a good representation of the flow. It has been shown that it is possible to compute naturally unsteady flows in the context of fluid–structure interaction by solving the unsteady RANS equations. For higher flow velocities, the maximum amplitudes were shown to agree fairly well with experiments.

Attaining the required spectral gap has proven to be elusive, however, due to the small time steps necessary to resolve all frequencies. Methods with a higher resolution, such as DNS or LES would address these problems but they will remain unfeasible in an engineering environment for the foreseeable future. Thus, a hybrid approach must be chosen. However, an improvement could not be achieved with the standard approach because it is based on a one-equation turbulence model that alone has failed to predict the unsteady behavior.

This well-known weakness of linear eddy-viscosity models for these kinds of flows, as already mentioned in the description of the models, is that they tend to overpredict the production of eddy-viscosity. This shortcoming can be overcome by a limitation of time and length scales, leading to an enhanced kind of DES approach for two-equation models that is currently under development. As the complexity of the flow discussed in this paper is too high this effect cannot be isolated and investigated here. Also, the effect of streamline curvature must be included separately and should be investigated in future work.

The coupling procedure was not thoroughly investigated, so its influence, as well as the influence of any transition modelling cannot be ruled out. An iterative coupling in time such as a predictor-corrector scheme will probably give better results for coarser time steps. As the numerical time step is very small with respect to the oscillation frequency with $170 < n < 200$ points per period in f_A, however, the chosen coupling of first-order accuracy is estimated to be sufficient. This also holds for the explicit discretization of the structure-mechanical differential equation itself, as a

higher order will not be profitable for the chosen coupling procedure (Piperno et al., 1995). Moreover, the deviations from experimental results in the Strouhal number occurred for the stationary body even without coupling.

The transition modelling cannot be validated for this test case due to the lack of experimental data; however, the mainly separated flow has likely undergone laminar turbulent transition at the sharp leading edge, which justifies the fully turbulent computations.

The 3-D results are not complete, and more research is needed. Initial results point to a lower damping in the flow with the possibility of a better representation of the frequencies. To further confirm this observation, more experimental data for this or similar cases will have to be gathered.

Summarizing, this fluid–structure interaction problem remains, though simple in geometry, a challenging and complex task that requires a careful explanation and substantiation of the methods chosen, and further research is considered necessary.

Acknowledgements

The 3-D calculations were carried out at the Konrad-Zuse-Zentrum Berlin (ZIB) on a Cray-T3E. This research is partly funded by Deutsche Forschungsgemeinschaft under the umbrella of the Sonderforschungsbereich 557, 'Beeinflussung komplexer turbulenter Scherströmungen' at the Technical University Berlin and partly by the CEC in the FLOMANIA project (Flow Physics Modeling—An Integrated Approach), which is a collaboration between Alenia, AEA, Bombardier, Dassault, EADS-CASA, EADS-Military Aircraft, EDF, NUMECA, DLR, FOI, IMFT, ONERA, Chalmers University, Imperial College, TU Berlin, UMIST and St. Petersburg State University. The project is funded by the European Union and administrated by the CEC, Research Directorate-General, Growth Programme, under Contract No. G4RD-CT2001-00613.

References

Anju, A., Maruoka, A., Kawahara, M., 1995. 2-D fluid–structure interaction problems by an arbitrary Lagrangian–Eulerian finite element method. Paper Department of Civil Engineering, Chuo University, Kasuga 1-13-27, Bunkyo-ku, Tokyo 112, Japan.

Bunge, U., Thiele, F., Rung, T., 2001. A two-dimensional sail in turbulent flow. Fluid Structure Interaction, Advances in Fluid Mechanics 30, 245–254.

Demirdžić, I., Perić, M., 1988. Space conservation law in finite volume calculations of fluid flow. International Journal for Numerical Methods in Fluids 8, 1037–1050.

Deniz, S., Staubli, T., 1997. Oscillating rectangular and octagonal profiles: interaction of leading- and trailing-edge vortex formation. Journal of Fluids and Structures 11, 3–31.

Dowell, E.H. (Ed.), 1995. A modern course in aeroelasticity. Solid mechanics and its applications, Vol. 32. Kluwer, Dordrecht.

Edwards, J.R., Chandra, S., 1996. Comparison of eddy-viscosity-transport turbulence models for three dimensional, shock-separated flowfields. AIAA Journal 34, 756–763.

Haase, W., Selmin, V., Winzell, B., 2002. Progress in computational flow–structure interaction. Results of the Project UNSI—Unsteady Viscous Flows in the Context of Fluid–Structure Interaction. Notes on Numerical Fluid Mechanics and Multidisciplinary Design, Vol. 81. Springer, Berlin.

Hémon, P., Santi, F., 2002. On the aeroelastic behaviour of rectangular cylinders in cross-flow. Journal of Fluids and Structures 16, 855–889.

Ikenouchi, M., Kakuno, T., Inoue, H., Sato, T., 1982. Fundamental investigation on wind resistant design of bridges. Mitsui Zosen Technical Review 116, 31–38.

Karki, K.C., Patankar, S.V., 1989. Pressure based calculation procedure for viscous flows at all speeds. AIAA Journal 27, 1167–1174.

Lübcke, H., Schmidt, S., Rung, T., Thiele, F., 2001. Comparison of LES and RANS in bluff-body flows. Journal of Wind Engineering and Industrial Aerodynamics 89, 1471–1485.

Menter, F., 1997. Eddy viscosity transport equations and their relation to the k–ε model. ASME Journal of Fluids Engineering 119, 876–884.

Moser, R.D., Moin, P., 1987. The effect of curvature on wall-bounded turbulent flows. Journal of Fluid Mechanics 175, 479–510.

Obi, S., Perić, M., Scheurer, M., 1991. Second moment calculation procedure for turbulent flows with collocated variable arrangement. AIAA Journal 29, 585–590.

Piperno, S., Farath, C., Larrouturou, B., 1995. Partitioned procedures for the transient solution of coupled aeroelastic problems. Computer Methods in Applied Mechanics and Engineering 124, 11–79.

Rung, T., 2000. Entwicklung anisotroper Wirbelzähigkeitsbeziehungen mit Hilfe von Projektions-techniken. Ph.D. Thesis, TU, Berlin.

Rung, T., Thiele, F., 1996. Computational modeling of complex boundary-layer flows. Proceedings of Ninth International Symposium on Transport Phenomena in Thermal-Fluid Engineering, Singapore, pp. 321–326.

Rung, T., Bunge, U., Schatz, M., Thiele, F., 2002. Restatement of the Spalart–Allmaras eddy-viscosity model in a strain-adaptive formulation. AIAA Journal 41 (7), 1396–1399.

Sakamoto, H., Takai, K., Aalam, M.M., Moriya, M., 2000. Suppression and characteristics of flow-induced vibration of rectangular prisms with various width-to-height ratios. Department of Mechanical Engineering, Kitami I.o.T., 165 Koen-Cho, Kitami, Hokkaido 090-8507, Japan.

Semler, C., Gentleman, W.C., Païdoussis, M.P., 1996. Numerical solutions of second order implicit non-linear ordinary differential equations. Journal of Sound and Vibration 195, 553–574.

Shur, M., Spalart, P.R., Strelets, S., Travin, A., 1999. Detached-eddy simulation of an airfoil at high angle of attack. Engineering Turbulence Modeling 4, 669–678.

Spalart, P.R., 2001. Young-person's guide to detached-eddy simulation grids. NASA Contractor Report 2001-211032.

Spalart, P.R., Allmaras, S.R., 1992. One equation turbulence model for aerodynamics. AIAA Paper 92-0339.

Strelets, S., 2001. Detached eddy simulation of massively separated flows. AIAA Paper 2001-0879

Wilcox, D.C., 1994. Simulation of transition with a two-equation turbulence model. AIAA Journal 32, 247–255.

Xue, L., 1998. Entwicklung eines effizienten parallelen Lösungsalgorithmus zur dreidimensionalen Simulation komplexer turbulenter Strömugen. Ph.D. Thesis, TU, Berlin.